International Journal of Heat and Mass Transfer 51 (2008) 6006–6017

Contents lists available at ScienceDirect

International Journal of Heat and Mass Transfer

journal homepage: www.elsevier.com/locate/ijhmt

Transient thermal and hydrodynamic model of flat heat pipe for the cooling of electronics components

R. Sonan [a], S. Harmand [a,*], J. Pellé [a], D. Leger [a], M. Fakès [b]

[a] LME, Université de Valenciennes et du Hainaut Cambrésis, 59313 Valenciennes, France
[b] Valeo Electrical Systems, 94017 Créteil, France

ARTICLE INFO

Article history:
Received 24 October 2007
Received in revised form 14 April 2008
Available online 6 August 2008

Keywords:
Electronics
Heat pipe
Phase change
Transient

ABSTRACT

The transient performance of a flat heat pipe (FHP) used to cool multiple electronics components, is presented in this paper. The fluid flows in both wick and vapor core were computed using a transient 2D hydrodynamic model (T2DHM). This model was coupled with a transient 3D thermal model (T3DTM) of the FHP wall, designed to calculate the heat transfer through the wall. An interesting procedure for solving the governing equations for the heat and mass transfers inside the FHP is proposed. The phase change mechanisms at the liquid–vapor interface are included in this procedure through the Clausius–Clapeyron law. During a start-up, the T2DHM is able to predict the velocity and pressure distribution of the liquid and the vapor, and thus the transient response of the FHP.

1. Introduction

Though new developments in electronics enhance the performance of electronic devices, these developments often mean the downsizing of the devices, which increases the heat flux generated by the electronic components. The dissipation of this flux inside the device can lead to such thermal problems as overheating, which can reduce the devices' performance levels as well as their lifespan. To avoid such problems, it is advisable to design effective cooling systems able to evacuate the considerable heat generated, thus maintaining the temperature of the components under their junction temperature [1]. Because heat pipes constitute highly reliable, efficient energy transport systems, they are increasingly being considered for cooling electronics. They can be an effective means of homogenizing the temperature from various heat sources (e.g., a spreader), or of transferring heat from heat sources (generally, electronic components) to heat sinks.

For this study, we investigated the possibility of using a flat heat pipe (FHP) as a spreader to cool multiple electronic components. Heat pipes have been known since the XIXth century but were not really used until the 1960s. Their numerous advantages have stimulated the development of many models over the last few years. Particular attention was first paid to steady-state models. In 2006, Lefèvre et al. [2] presented an analytical solution for liquid and vapor flows as well as the temperature distribution inside a flat micro heat pipe, under the action of three electronic components. This model is devoted to the steady-state performance of flat heat pipes and is based on the coupling of the fluid flows and heat transfer processes. It was assumed that the liquid and vapour flows are governed by simplified transport equations as Darcy's law. The authors pointed out that conduction though the wall and wick is seen to play a significant role in determining the temperature distribution in FHP.

In this work the similar approach developed in Lefèvre et al. [2] is adopted and extended to analyze the performance of a FHP subjected to heating with multiple electronic components during a transient period. A combinatory model, coupling a transient thermal model with a transient hydrodynamic model is performed. The thermal model distinguishes the part of the heat flux transferred via heat conduction through the FHP wall from the heat transferred via phase changes. The mass and heat transfers related to the liquid–vapor phase change define the thermal model's boundary conditions. We extended the hydrodynamic model proposed by Huang et al. [3] for the FHP wick in order to determine the transient liquid flow. We developed a similar model to predict the vapor flow in the vapor core during FHP operations. The hydrodynamic model is coupled to the thermal model through the mass flux of evaporation–condensation, which occurs in a mass conservation equation.

2. Mathematical models

The FHP considered in this study is a copper–water heat pipe. Situated within the liquid flow, the wick structure is a porous media characterized by its permeability K, its porosity ε and its effective pore radius r_{eq}. The geometry and the scheme of the FHP considered here are shown in Figs. 1 and 2. As shown, the

* Corresponding author. Tel.: +33 327 511 974; fax: +33 327 511 961.
E-mail address: souad.harmand@univ-valenciennes.fr (S. Harmand).

0017-9310/$ - see front matter © 2008 Elsevier Ltd. All rights reserved.
doi:10.1016/j.ijheatmasstransfer.2008.04.071

Nomenclature

Cp	specific heat capacity, J kg^{-1} K^{-1}
H	thickness, m
h	heat transfer coefficient W K^{-1} m^{-2}
h_{fg}	latent heat of vaporisation, J kg^{-1}
K	permeability, m^2
L	length of the FHP, m
p	pressure, Pa
r	pore radius, m
T	temperature, K
t	time, s
u	velocity along the x axis, m s^{-1}
V	velocity vector, m s^{-1}
v	velocity along the y axis, m s^{-1}
μ	dynamic viscosity, Pa s
ρ	density, kg m^{-3}
σ	surface tension, N m^{-1}
ϕ	heat flux, W m^{-2}

Subscripts

0	initial, reference
a	ambient
cd	condenser
Ei	electronic component
eq	equivalent
l	liquid
max	maximum
s	solid, wall
x, y, z	coordinates, m

Greek symbols

α	mass flow rate per unit volume, kg s^{-1} m^{-3}
ε	porosity of the wick
λ	thermal conductivity, W K^{-1} m^{-1}
sat	saturation
w	wick
v	vapor
x, y, z	coordinate references

electronic components are located at different places on the FHP's upper surface. The heat flux generated by these electronic components corresponds to a uniformly-applied heat source at evaporators (area where the components are place). Condensers, on the other hand, are cold sources or heat sinks. They ensure that the heat flux is evacuated outside through the FHP wall. Though both evaporators and condensers are mounted on the FHP surface, the surrounding surface is adiabatic.

The modelling was done in two main steps. First, a Transient 3D Thermal Model (T3DTM) was developed to define the transient heat transfers, both from the electronic components to the fluid and from the fluid to the condensers through the FHP wall. In the FHP, these heat transfers cause the liquid to evaporate in the evaporators and the vapor to condense in the condensers. Then, a Transient 2D Hydrodynamic Model (T2DHM) was developed to characterize the fluid flow in both the wick and the vapor core. In this model, the flow is assumed to be laminar and to occur only in the x and y directions.

2.1. Transient 3D thermal model (T3DTM)

The FHP wall is composed of a material with constant thermophysical properties, denoted λ_s, ρ_s, Cp_s, and a thickness H_z. It is assumed that all surfaces of the wall, except those where evaporators and condensers are placed, are perfectly insulated. The model characterizes the conduction heat transfers throughout a start-up. The heat flux, released by the electronic components on the FHP surface, is transferred to the porous media where it causes the liquid to evaporate. In the condensers, the vapor condenses, and the heat released is evacuated outside through the FHP wall. These heat transfer mechanisms are defined by the 3D transient heat conduction equation as:

$$(\rho \mathrm{Cp})_s \frac{\partial T}{\partial t} - \lambda_s \left(\frac{\partial^2 T}{\partial x^2} + \frac{\partial^2 T}{\partial y^2} + \frac{\partial^2 T}{\partial z^2} \right) = 0 \tag{1}$$

The boundary conditions are, Fig. 2:

$$\left.\frac{\partial T}{\partial x}\right|_{x=0} = \left.\frac{\partial T}{\partial x}\right|_{x=Lx} = 0 \tag{2}$$

$$\left.\frac{\partial T}{\partial y}\right|_{y=0} = \left.\frac{\partial T}{\partial y}\right|_{y=Ly} = 0 \tag{3}$$

$$\lambda_s \left.\frac{\partial T}{\partial z}\right|_{z=0} = h_{eq}(T|_{z=0} - T_{sat}) \tag{4}$$

$$\lambda_s \left.\frac{\partial T}{\partial z}\right|_{z=Lz} = \begin{cases} \varphi_{Ei} : & \text{evaporator area} \\ 0 : & \text{adiabatic area} \\ h_{cd}(T|_{z=Lz} - T_a) : & \text{condenser area} \end{cases} \tag{5}$$

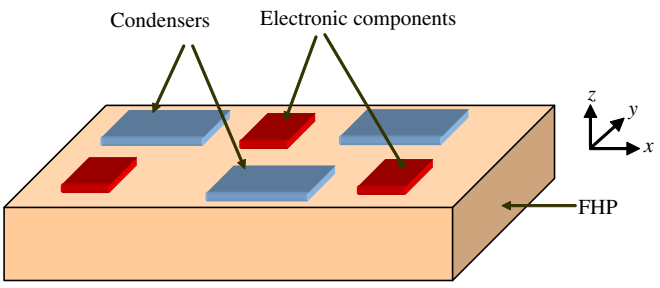

Fig. 1. Schematic drawing of a FHP, showing heat sources and heat sinks mounted on the same surface.

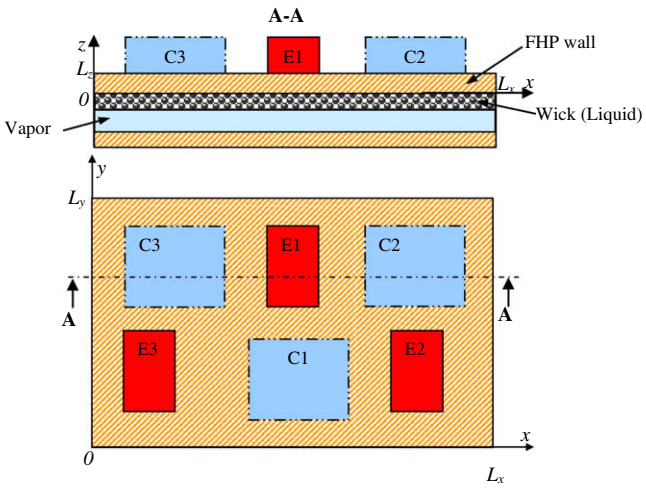

Fig. 2. Schematic drawing of a FHP along the (z, x) and (y, x) planes.

In the condenser area, the heat convection between FHP wall and the ambient environment is characterized by the transfer coefficient h_{cd} (Eq. (5)). At the wick-wall interface, heat exchanges are defined by the Fourier boundary condition (Eq. (4)), where h_{eq} is the heat transfer coefficient between the FHP wall and the fluid at the saturation temperature T_{sat} supposed to be dependent both in time and in space (i.e., $T_{sat} = T_{sat}(x, y, t)$).

The heat transfer coefficient h_{eq} is equivalent to the thermal conductance of the porous media filled with liquid [2]. In addition, the following initial conditions are imposed:

$$t = t_0, T(x,y,z,t_0) = T_{sat}(x,y,t_0) = T_a \tag{6}$$

With the T3DTM described above, the heat transfer through the FHP wall is known. Therefore, to calculate the fluid flow resulting from the heat transfer mechanisms, the T2DHM described in the following section is used for both liquids and vapor.

2.2. Transient 2D Hydrodynamic Model (T2DHM)

The hydrodynamic models proposed for the wick by Lefèvre et al. [2] and Huang [3] assume that the liquid flow within the porous media is expressed by Darcy's law. However, in a transient state, this law is not necessarily valid. Thus, we developed a T2DHM model for predicting the liquid and vapor flows in the FHP during a start-up operation. Knowing the pressure distribution makes it possible to determine the temporal evolution of the pressure losses, and thus the FHP's transient capillary limit. Since the wick thickness H_w and the vapor thickness H_v are small compared to the model's L_x and L_y dimensions, the fluid flows are assumed to be 2D. Thus, the velocity along the z direction can be ignored [2,3].

2.3. T2DHM for liquid

It is assumed that the FHP wick is constantly filled with liquid. The modelling procedure consists of integrating the mass conservation equation into the momentum equation to obtain a second-order differential equation, in which pressure is not coupled to velocity. This provides a solution to the pressure-velocity coupling in transient flows.

To establish the mass conservation equation, a liquid control volume, $dV_l = \partial x \times \partial y \times H_w$, in the wick region, is considered as shown in the following diagram.

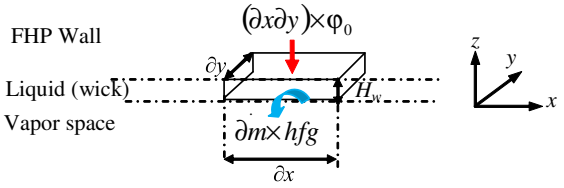

Where φ_0 denotes the heat flux at the wall – wick interface, calculated with the previous thermal model T3DTM, stated as: $\varphi_0 = h_{eq}(T|_{z=0} - T_{sat})$.

$\partial\dot{m}$ denotes the mass flow rate of evaporation at the given control volume. The mass conservation at the given liquid control volume is expressed as:

$$\partial\dot{m} = \partial\dot{m}_x + \partial\dot{m}_y = \rho_l \partial y H_w \partial u_l + \rho_l \partial x H_w \partial v_l \tag{7}$$

Assuming a quasi - instantaneous approach, the energy balance at the given control volume is expressed as: $\varphi_0 \partial x \partial y = \partial\dot{m} h_{fg}$.

Applying the energy balance to the mass conservation equation leads to express the liquid mass conservation equation as [2,3]:

$$\frac{\partial u_l}{\partial x} + \frac{\partial v_l}{\partial y} = \frac{\varphi_{z0}}{\rho_l h_{fg} H_w} = \frac{\alpha_l}{\rho_l} \text{ with } \alpha_l = \frac{h_{eq}}{h_{fg} H_w}(T|_{z0} - T_{sat}) \tag{8}$$

Where $T|_{z=0}$ is the temperature at the wick-wall interface, as determined by the T3DTM model, and α_l is the mass flow rate of evaporating liquids, which depends on T_{sat}, the fluid saturation temperature.

The flow of liquids through the wick is governed by the porous media momentum equation [4]:

$$\frac{\rho_l}{\varepsilon}\left(\frac{\partial u_l}{\partial t} + u_l\frac{\partial u_l}{\partial x} + v_l\frac{\partial u_l}{\partial y}\right) = -\frac{\partial p_l}{\partial x} - \frac{\mu_l}{K}u_l \tag{9}$$

$$\frac{\rho_l}{\varepsilon}\left(\frac{\partial v_l}{\partial t} + u_l\frac{\partial v_l}{\partial x} + v_l\frac{\partial v_l}{\partial y}\right) = -\frac{\partial p_l}{\partial y} - \frac{\mu_l}{K}v_l \tag{10}$$

By differentiating between Eqs. (9) and (10) according to x and y, respectively, and summing the resulting derivates, the following equation is obtained:

$$\frac{\partial^2 p_l}{\partial x^2} + \frac{\partial^2 p_l}{\partial y^2} = -\frac{\mu_l}{K}\left(\frac{\partial u_l}{\partial x} + \frac{\partial v_l}{\partial y}\right) - \frac{\rho_l}{\varepsilon}\left[\frac{\partial}{\partial t}\left(\frac{\partial u_l}{\partial x} + \frac{\partial v_l}{\partial y}\right) + \left(\frac{\partial u_l}{\partial x} + \frac{\partial v_l}{\partial y}\right)^2 + u_l\frac{\partial}{\partial x}\left(\frac{\partial u_l}{\partial x} + \frac{\partial v_l}{\partial y}\right) + v_l\frac{\partial}{\partial y}\left(\frac{\partial u_l}{\partial x} + \frac{\partial v_l}{\partial y}\right)\right] \tag{11}$$

Applying the mass conservation equation to Eq. (11) yields Eq. (12):

$$\frac{\partial^2 p_l}{\partial x^2} + \frac{\partial^2 p_l}{\partial y^2} = -\frac{\mu_l}{K\rho_l}\alpha_l - \frac{1}{\varepsilon}\left(\frac{\partial \alpha_l}{\partial t} + \frac{\alpha_l^2}{\rho_l} + u_l\frac{\partial \alpha_l}{\partial x} + v_l\frac{\partial \alpha_l}{\partial y}\right) \tag{12}$$

In the present formulation, it is assumed that the total derivative of the mass flow rate α is equal to its partial derivative according to time, which can be expressed as:

$$\frac{D\alpha_l}{Dt} \approx \frac{\partial \alpha_l}{\partial t} \text{ with the approximation} : \frac{\partial \alpha_l}{\partial t} \gg u_l\frac{\partial \alpha_l}{\partial x} + v_l\frac{\partial \alpha_l}{\partial y} \tag{13}$$

This assumption is justified by the fact that the term $u_l\frac{\partial \alpha_l}{\partial x} + v_l\frac{\partial \alpha_l}{\partial y}$ is always negligible compared to $\frac{\partial \alpha_l}{\partial t}$. The computational algorithm developed during this study allowed this approximation to be validated (Table 3). Applying this assumption to Eq. (12) produces the final pressure equation, expressed as:

$$\frac{\partial^2 p_l}{\partial x^2} + \frac{\partial^2 p_l}{\partial y^2} = -\frac{\mu_l}{K\rho_l}\alpha_l - \frac{1}{\varepsilon}\left(\frac{\partial \alpha_l}{\partial t} + \frac{\alpha_l^2}{\rho_l}\right) \tag{14}$$

The steady-state pressure equation used in the models proposed by Lefèvre et al. [2] and Huang [3] is part of Eq. (14), and is recognized as: $\frac{\partial^2 p_l}{\partial x^2} + \frac{\partial^2 p_l}{\partial y^2} = -\frac{\mu_l}{K\rho_l}\alpha_l$. In those models, the contribution of the term $\frac{1}{\varepsilon}\frac{\alpha_l^2}{\rho_l}$ is neglected. But in our model that term is taking to account.

The boundary conditions for the pressure are [2,3]:

$$\left.\frac{\partial p_l}{\partial x}\right|_{x=0} = \left.\frac{\partial p_l}{\partial x}\right|_{x=Lx} = \left.\frac{\partial p_l}{\partial y}\right|_{y=0} = \left.\frac{\partial p_l}{\partial y}\right|_{y=Ly} = 0 \tag{15}$$

Now, since the liquid pressure distribution is well known, it is easy to calculate the velocity field using Eqs. (9) and (10). The boundary conditions for the velocity field are: $u_l|_{x=0} = u_l\ |_{x=Lx} = v_l|_{y=0} = v_l|_{y=Ly} = 0$.

The initial conditions were assumed for a saturated fluid and uniform pressure distribution. The initial velocities were also assumed equal to zero. The initial conditions are stated below:

$$p_l(t = t_0) = p_{sat}(T(t = t_0)), u_l(t = t_0) = v_l(t = t_0) = 0 \tag{16}$$

2.4. T2DHM for vapor

At the vapor core, a similar approach to the one used for the liquid was used to determine the pressure and velocity fields. The

vapor flow along the z direction is assumed to be neglected. The mass vapor balance is expressed as [2]:

$$\frac{\partial u_v}{\partial x}+\frac{\partial v_v}{\partial y}=-\frac{\alpha_v}{\rho_v},\alpha_v=\frac{h_{eq}}{h_{fg}H_v}(T|_{z=0}-T_{sat}) \tag{17}$$

where α_v is the mass flow rate of the vapor condensation. The mass flow depends on the wall temperature and the vapor saturation temperature.

Assuming that the vapor flow is laminar between two parallel plates, the vapor velocity profile can be found using Bejan's formulation [5]:

$$\mu_v\left(\frac{\partial^2 u_v}{\partial x^2}+\frac{\partial^2 u_v}{\partial y^2}\right)\approx-\frac{12\mu_v}{H_v^2}u_v\text{et}\mu_v\left(\frac{\partial^2 v_v}{\partial x^2}+\frac{\partial^2 v_v}{\partial y^2}\right)\approx-\frac{12\mu_v}{H_v^2}v_v$$

Based on this formulation, the momentum equation can then be simplified as:

$$\rho_v\left(\frac{\partial u_v}{\partial t}+u_v\frac{\partial u_v}{\partial x}+v_v\frac{\partial u_v}{\partial y}\right)=-\frac{\partial p_v}{\partial x}-\frac{12\mu_v}{H_v^2}u_v \tag{18}$$

$$\rho_v\left(\frac{\partial v_v}{\partial t}+u_v\frac{\partial v_v}{\partial x}+v_v\frac{\partial v_v}{\partial y}\right)=-\frac{\partial p_v}{\partial y}-\frac{12\mu_v}{H_v^2}v_v \tag{19}$$

Applying the previous method for liquids to Eqs. (18) and (19) leads to the vapor pressure distribution, expressed as:

$$\frac{\partial^2 p_v}{\partial x^2}+\frac{\partial^2 p_v}{\partial y^2}=\frac{12\mu_v}{\rho_v H_v^2}\alpha_v+\left(\frac{\partial\alpha_v}{\partial t}-\frac{\alpha_v^2}{\rho_v}\right) \tag{20}$$

Supposing the second term on the right side of Eq. (20) is negligible allows the easy recognition of the governing equations of the Lefèvre et al. [2] and Huang [3] models for the vapor core at the steady state, expressed as: $\frac{\partial^2 p_v}{\partial x^2}+\frac{\partial^2 p_v}{\partial y^2}=\frac{12\mu_v}{\rho_v H_v^2}\alpha_v$.

The following boundary conditions are imposed on the vapor domain [2]:

$$\left.\frac{\partial p_v}{\partial x}\right|_{x=0}=\left.\frac{\partial p_v}{\partial x}\right|_{x=Lx}=\left.\frac{\partial p_v}{\partial y}\right|_{y=0}=\left.\frac{\partial p_v}{\partial y}\right|_{y=Ly}=0 \tag{21}$$

Eqs. (18) and (19) allow the vapor velocity field to be determined, based on the calculation of the pressure distribution as shown above. The boundary conditions for velocity are [6]:

$$u_l|_{x=0}=u_l|_{x=Lx}=v_l|_{y=0}=v_l|_{y=Ly}=0 \tag{22}$$

The initial conditions can be expressed as:

$$\begin{aligned}p_v&=p_{sat}(T_{sat}(x,y,t_0))\\ u_v&=v_v=0\end{aligned} \tag{23}$$

To simplify the analysis, it was assumed that the vapor had reached the saturation condition ($T_v = T_{sat}$, $p_v = p_{sat}$), so that the saturation

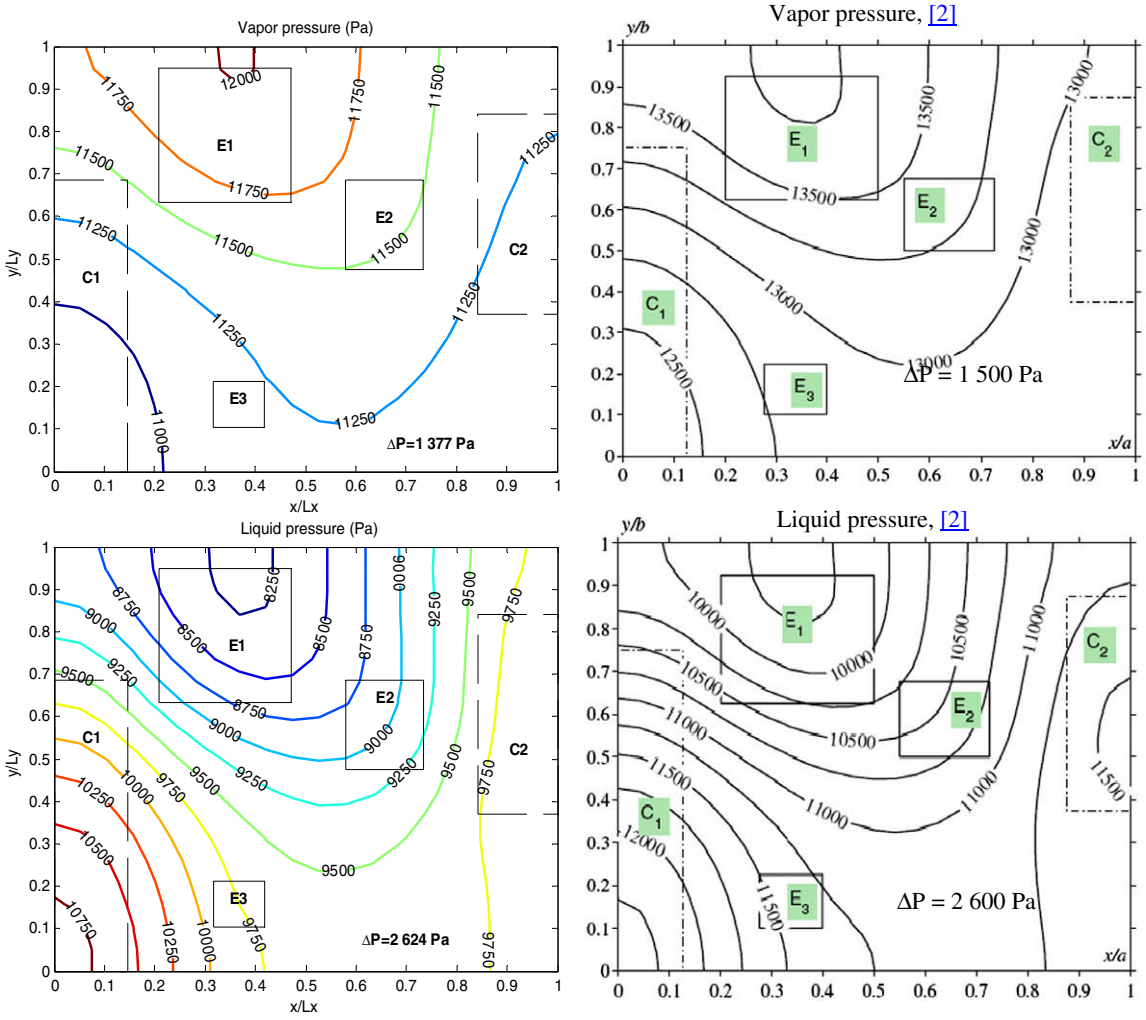

Fig. 3. Vapor and liquid pressure ditribution (Pa): (a) our results and (b) the results of Lefèvre et al. [2].

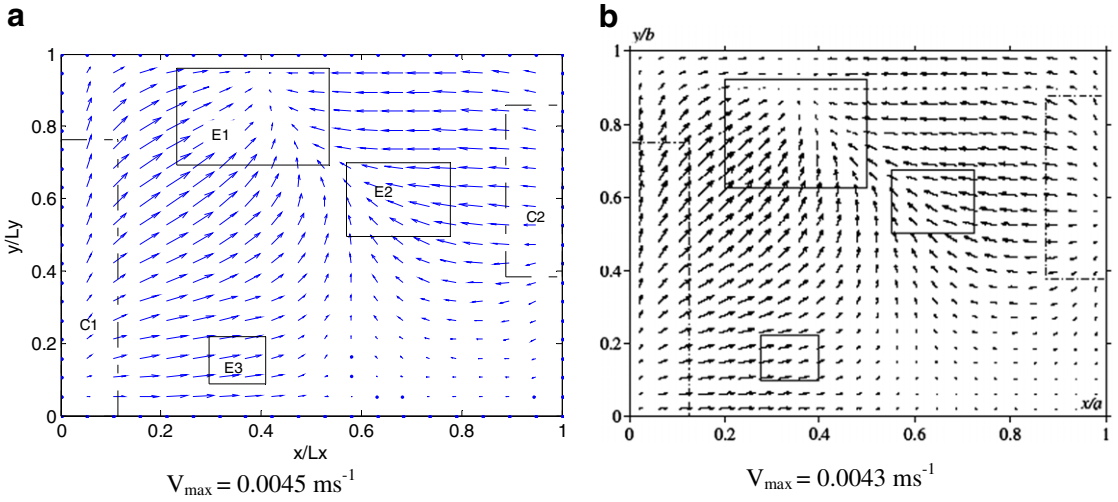

Fig. 4. Liquid velocity (m/s), (a) our results and (b) the results of Lefèvre et al. [2].

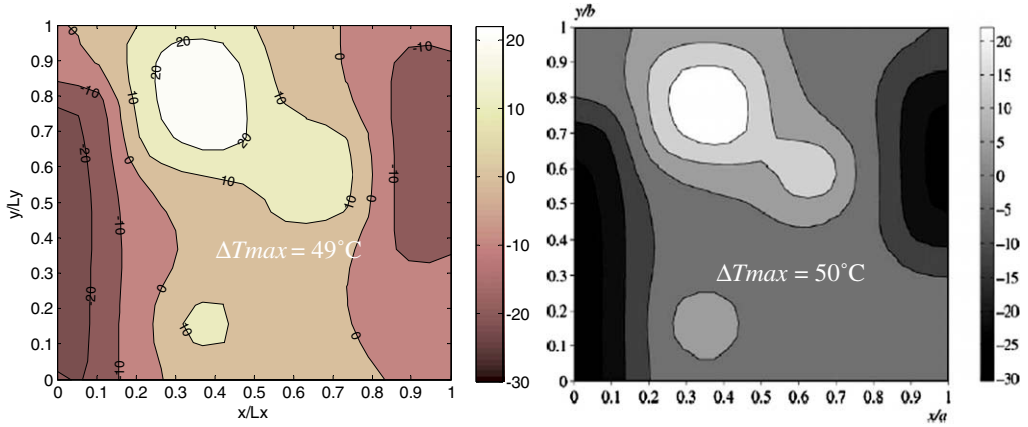

Fig. 5. Temperature difference (Ts-Tsat) (K): (a) our results and (b) the results of Lefèvre et al [2].

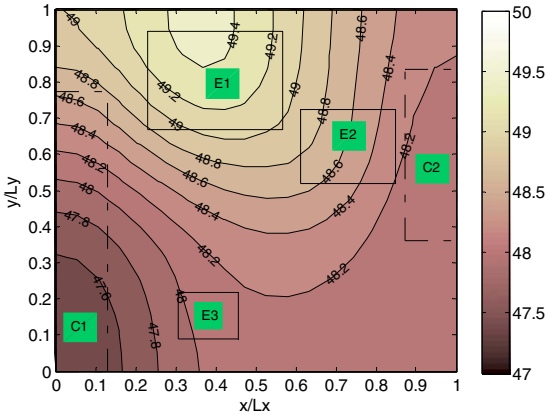

Fig. 6. Saturation temperature distribution (°C), as predicted by our model.

temperature could be calculated using the Clausius–Clapeyron equation:

$$\frac{\Delta T_{sat}}{T_{sat}} = \left(\frac{\rho_v^{-1} - \rho_l^{-1}}{h_{fg}}\right)\Delta p_v \qquad (24)$$

Table 1
FHP size considered for the simulation in the Section 3.2

Length (L_x), mm	30
Width (L_y), mm	20
Thickness ($H = 2L_z+H_l+H_v$), mm	2.6
Wall thickness (L_z), mm	1
Wick thickness (H_l), mm	0.2

3. Results and discussion

In order to capture the transient variations with minimal round-off errors, and to simplify the computational scheme, an implicit Euler computational procedure was employed for time differencing. The governing equations were discretized using the finite difference method, and the nonlinear terms in the momentum equations were discretized according the linearization method suggested by Fletcher [7]. The computational code was written with Matlab®. The time step and spatial grid size required for fast convergence was determined through trial and error. Temperature, pressure and velocity distributions were calculated successively. The following section compares the results of our model with the results available in the literature.

Table 2
Thermo physical properties of the FHP material and the working fluid [8]

Properties	Wall (copper)	Vapour (water)	Liquid (water)	Wick (screen)
Density, kgm^{-3}	8978	0.0173	988.7	–
Specific heat, $Jkg^{-1}K^{-1}$	381	1874	4182	–
Thermal conductivity, $Wm^{-1}K^{-1}$	387.6	–	0.602	1.3
Dynamic viscosity, Pas	–	$8.85\ 10^{-6}$	0.001	–
Latent heat, $kJkg^{-1}$	–	2453.8		–
Porosity	–	–	–	0.733
Permeability, m^2	–	–	–	$0.52\ 10^{-10}$
Equivalent pore radius, m	–	–	–	$58\ 10^{-6}$

Table 3
Numerical results proving the main assumption of the model (Eq. (13))

t, s	0.1	0.3	1.4	2
$\max\left[\rho_l\left(\frac{\partial\alpha_l}{\partial t}\right)\right]$, s^{-1}	10.1×10^5	$5.2\ 10^5$	$1.5\ 10^5$	1.4×10^5
$\max\left[\rho_l\left(u_l\frac{\partial\alpha_l}{\partial x}+v_l\frac{\partial\alpha_l}{\partial y}\right)\right]$, s^{-1}	2.6×10^4	6.9×10^4	1.5×10^4	0.2×10^4
$\max\left[\rho_v\frac{\partial\alpha_v}{\partial t}\right]$, s^{-1}	8.7	4.5	1.3	1.2
$\max\left[\rho_v\left(u_v\frac{\partial\alpha_v}{\partial x}+v_v\frac{\partial\alpha_v}{\partial y}\right)\right]$, s^{-1}	1.2	0.7	0.1	1.4×10^{-2}

3.1. Model validation through comparison with the literature

The results of our model are compared below to the analytical results published by Lefèvre et al. [2] for a steady-state operation. The aim here is to use the model of Lefèvre [2] as a test-case in order to validate our model at steady state, while waiting the assessment of the model on experimental results. Indeed, experimental investigations are ongoing and better validation will be performed.

The heat pipe considered was a flat copper heat pipe filled with water, measuring $40\times40\times0.9\ mm^3$. The wall, wick and vapor thicknesses were, respectively, 265, 140 and 230 μm. Three electronic components (E_1, E_2 and E_3) and two heat sinks (C_1 and C_2) were tested, as shown in Fig. 3. The heat sources (electronics components) all generated the same heat flux: $35\ Wcm^{-2}$. In their work, Lefevère et al. used Neumann boundary conditions at the condensers area and the saturation temperature, T_{sat}, is fixed equal to 50 °C. The mean difference with our model is that our formulation allows the calculation of the temperature T_{sat} instead of imposed it as these authors done. In order to simulate the same heat pipe operation, the value of the heat exchange coefficient at condensers, h_{cd}, is determined by such that T_{sat} tends, in average point of view, to equalize the value of 50 °C. Therefore, the equivalent exchange coefficient was about $h_{cd}=4500\ W/K\ m^2$.

Fig. 3 shows the results obtained by our model at a steady state compared with those published by Lefèvre et al. [2]. As this figure shows, the results of our model correspond well to those of these authors. Indeed, the vapor pressure distribution of our model (Fig. 3a) is similar to the one reported by Lefèvre et al. (Fig. 3b). They obtained a drop in vapor pressure of about $\Delta P_v = 1\ 500$ Pa, while our model predicts slightly lower, $\Delta P_v = 1\ 377$ Pa. In the liquid flow, the model predicts $\Delta P_l = 2\ 624$ Pa, when the authors [2] obtained $\Delta P_l = 2600$ Pa. Thus the maximum capillary pressure is about $\Delta P_c = 4001$ with our formulation and about $\Delta P_{c,max} = 4$

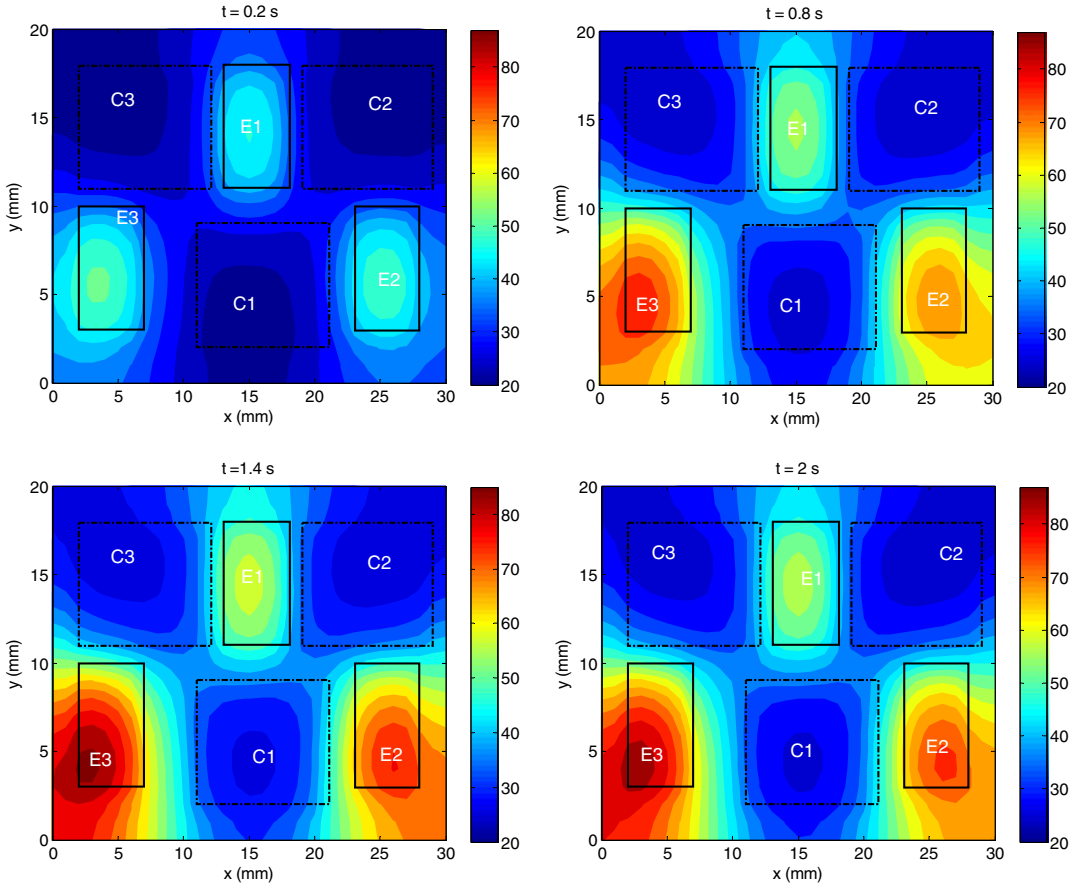

Fig. 7. Transient temperature response of the solid copper plate (°C), at the top side.

100 Pa with the model of these authors. That represents a slight difference of 2.4%.

The velocity fields obtained with our model (Fig. 4a) also correspond well to those of Lefèvre [2] (Fig. 4b), with a relative difference of about 4.4%.

At steady state, the wall temperature determined by our thermal model is close to those of Lefèvre [2]. Fig. 5 shows the temperature difference between the wall (where the electronic components are placed) and the saturation temperature. With our model, the maximum temperature difference ΔT_{max}, between the electronic component E_1 and the condenser C_1 or C_2, is about 49 K (Fig. 5a). Lefèvre et al. [2] obtained $\Delta T_{max} = 50$ K (Fig. 5b), that leads to an absolute deviation of 1 K.

The variation in the Lefèvre study is due to the authors' assumption that the saturation temperature is constant, about 50 °C [2]. However, because T_{sat} depends on the distribution of the heat sinks in the heat pipe wall, this assumption is not totally realistic. Thus, the dependence of the saturation temperature on surface space must also be taken in to consideration, as we did in our model (Fig. 6).

As these results shown, the results from our model correspond well to those published in the literature. Given this validation, we simulated the cooling of multiple electronic components using a FHP. The T3DTM and T2DHM models were used to predict the transient performance of the FHP during the start-up operation, in terms of temperature pressure and velocity. An experimental investigation is already predicted and it will soon be performed. That will provide a better validation by comparing the measured data to the model results.

3.2. FHP cooling of multiple electronic components

In this last section, we describe the results of simulations, run with the FHP shown in Figs. 1 and 2. The FHP was used to cool three electronic components (E_1, E_2, and E_3) during a start-up operation. Each component was assumed to generate a heat flux $\phi_{Ei} = 200$

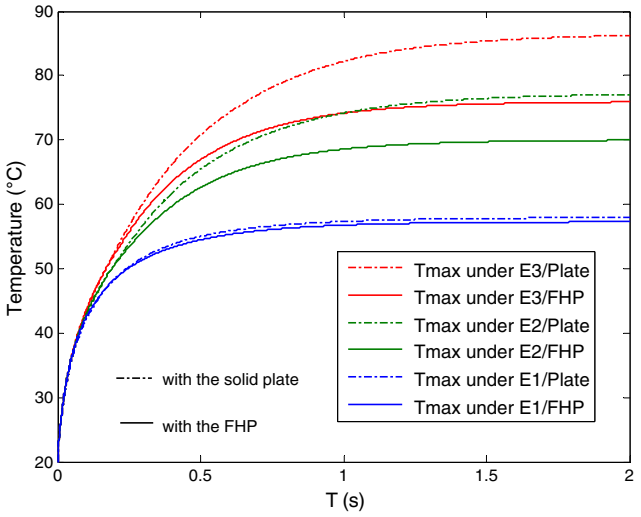

Fig. 9. Transient temperature evolution of the electronic components for the FHP case (bold lines) and for the solid copper plate (dotted lines).

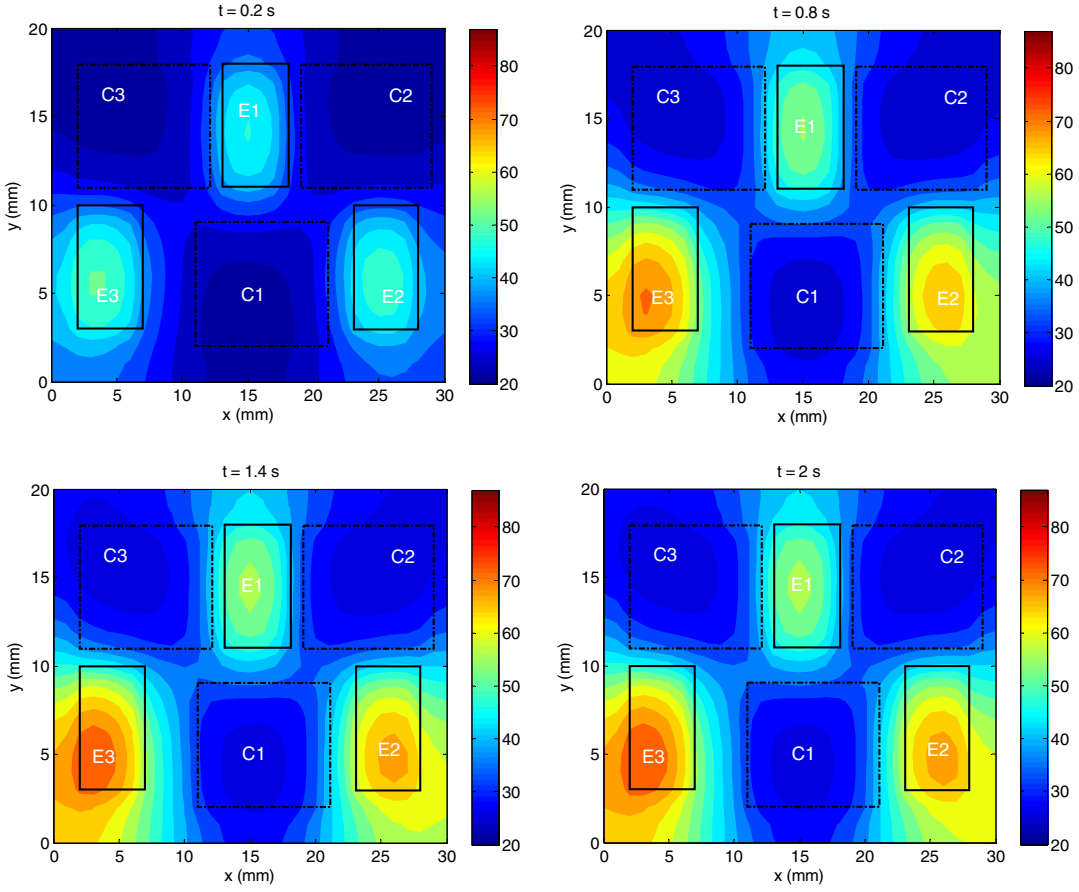

Fig. 8. Transient temperature response of the FHP (°C), at the top side.

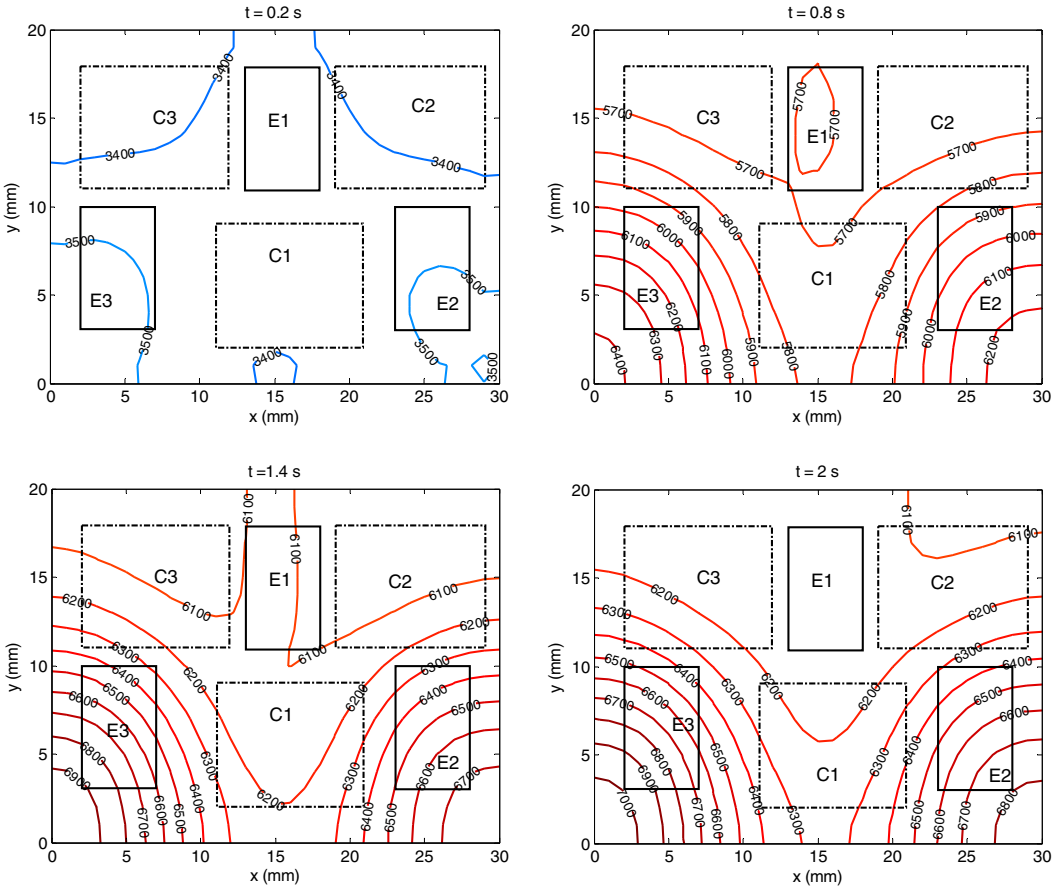

Fig. 10. Vapor pressure distribution (Pa) at the different elapsed times considered.

Wcm^{-2} during 2 s. Three condensers (C_1, C_2 and C_3) were placed on the same wall as the components (Fig. 1), with an equivalent heat transfer coefficient h_{cd} = 9 2769 $WK^{-1}m^{-2}$ at a reference temperature T_a = 20 °C. The initial temperature was about 20 °C, corresponding to a saturation temperature of 2 336.8 Pa. The heat transfer coefficient at the wick-wall interface was set at h_{eq} = 6 500 $WK^{-1}m^{-2}$.

The following tables provide the details about the FHP size (Table 1) and its thermo-physical properties (Table 2). A variety of tests were performed to establish time-step and mesh independence. As the result of the grid independence study, the $31 \times 21 \times 5$ ($x \times y \times z$) mesh was used for the thermal model. The wick and vapor regions include the same grid point $31 \times 21 \times 1$ ($x \times y \times z$). The time step of 10^{-3} s was adequate to ensure convergence and stability of the calculations.

According the numerical results obtained (Table 3), the main assumption of our model – the inequality expressed in Eq. (13) according to our hypothesis – is clearly validated.

To demonstrate the potential capability of the FHP as a thermal spreader for cooling electronic components, we compared our results with those from a numerical analysis performed on a solid copper plate, whose mass was equivalent to that of the FHP (m_{eq} = 5.8 g). The plate was subjected to the same heat flux, initial conditions and boundary conditions as the FHP.

The transient temperature response of the solid copper plate is presented in Fig. 7 and the response for the upper surface of the FHP, where the electronic components were placed, is presented in Fig. 8. The bold rectangles indicate the location of the electronic components and the dotted rectangles indicate the location of the condensers.

The maximum temperature difference ΔT_{max} between the hottest component E_3 and the condensers C_3 or C_2, was higher on the copper plate (Fig. 7) than on the FHP (Fig. 8). For instance, at t = 2 s, ΔT_{max} was about 61 K for the copper plate, but only 50 K for the FHP, which corresponds to a decrease of 11 K.

According to these results, the heat pipe is able to generate a more uniform temperature distribution across the x–y plane than the solid copper plate, which is subjected only to pure conduction. Thus, it appears that pure conduction is less efficient and not as well adapted to distributing the non-uniform heat input produced by the electronic components. The evaporation and condensation process in the FHP causes the rapid transport of energy from the evaporator to the condenser, and spreads this energy out evenly via the liquid flow through the wick structure. Thus, as is obvious from the results presented in Figs. 7 and 8, the heat is more uniformly spread throughout the FHP, which reduces the area of temperature concentration and makes the wall temperature distribution tend to be uniform.

According to the heat source distribution over the FHP surface, E_3 is the hottest electronic component because it is located far away from the condensers. The proximity of the component E_1 to the heat sinks C_2 and C_3 could explain why the E_1 component is colder than the E_2 and E_3 components. Fig. 9 shows a plot of the time evolution of the maximum temperature over these electronic components for the FHP case (bold lines) and the copper plate case (dotted lines). In both cases, the hottest component is E_3 and the coolest is E_1. At the end of the start-up cycle (t = 2 s), the maximum temperature over E_3 is about 86 °C for the solid plate but it is only about 75 °C for the FHP. Thus, using the FHP leads to a cooling profit of 11 K. Similarly, with the E_2 component, cooling by FHP allows

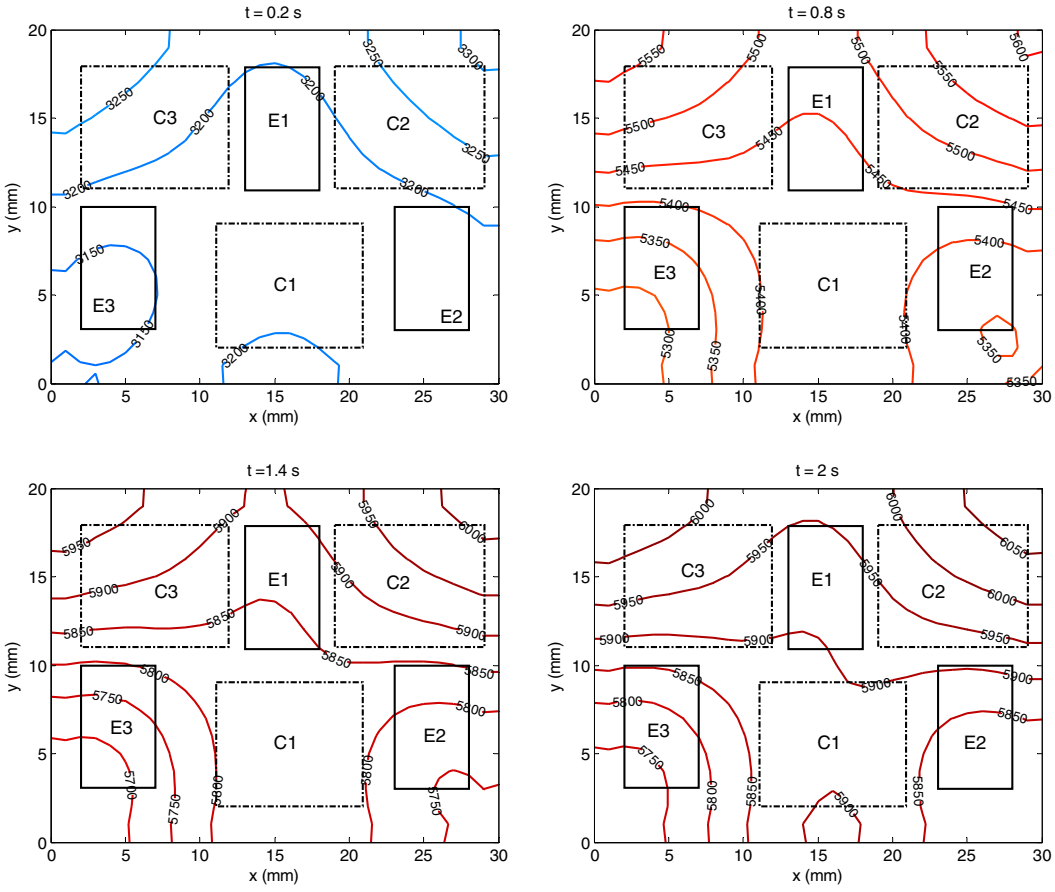

Fig. 11. Liquid pressure distribution (Pa) at the different elapsed times considered.

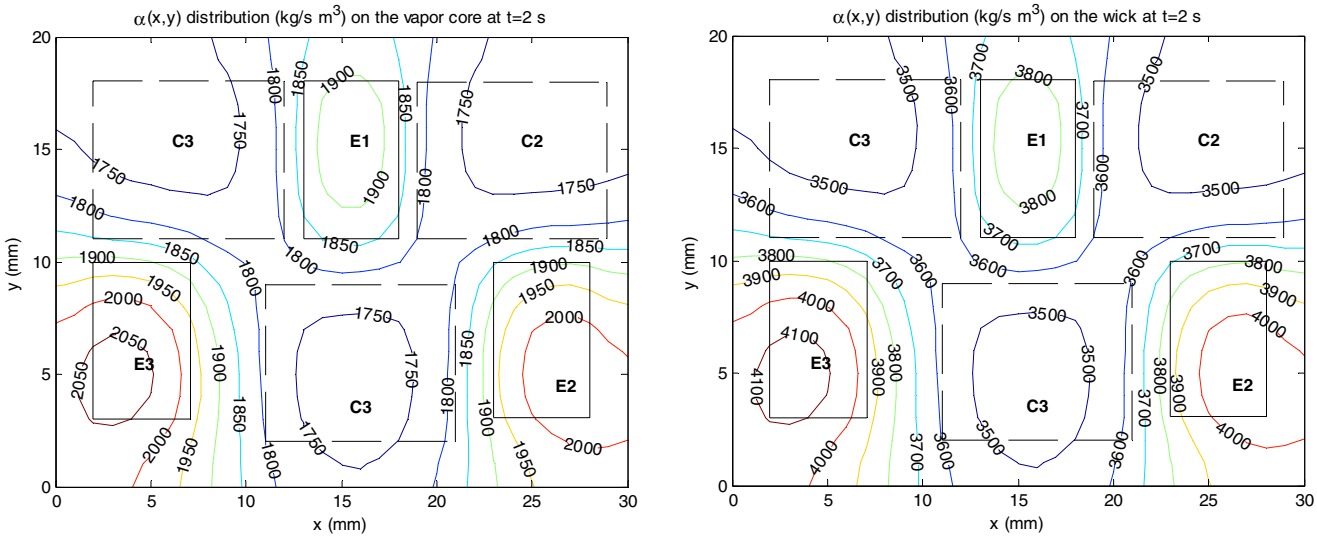

Fig. 12. The field of flow rate (kg/s m^3), α (x,y) at $t = 2$ s.

the maximum temperature to be decreased from 77 to 69 °C, which corresponds to a drop of 8 K compared with the cooling by solid copper plate. The profit is negligible (0.6 K) for the E_1 component, due to the close proximity of condensers C_3 and C_2 that channel the heat flux away.

The vapor and liquid pressure distributions in the FHP are presented in Figs. 10 and 11, respectively, at elapsed times of 0.2, 0.8, 1.4 and 2 s. As Fig. 10 shows, at any time, the vapor pressure distribution follows the heat sources distribution on the heat pipe wall. The vapor pressure reached important value at the side where the electronic components E_2 and E_3 are placed, compared to the side where condensers are placed (C_2 and C_3). Indeed, under the electronic components, the flow rate of evaporation increases, whereas it decreases under condensers, Fig. 12.

Compared to the vapor pressure distribution, the liquid pressure in the wick follows a reverse distribution (Fig. 11). Indeed, liquid evaporation and vapor condensation in the FHP operation occur in a reverse but quasi-instantaneous manner.

Knowing the fluid pressure distributions in the FHP allows the drop in the liquid pressure (ΔP_l) and in the vapor pressure (ΔP_v) to be assessed precisely, which in turn makes precise assessments of the capillary pressure inside the FHP possible. This last type of pressure corresponds to the sum of pressure losses along the vapor–liquid path necessary to allow the fluid to circulate inside the heat pipe. The capillary pressure is expressed as $\Delta P_c = \Delta P_v + \Delta P_l$. In order for the heat pipe to operate properly, it is absolutely necessary for the maximum capillary pressure head ($\Delta P_{c,max}$) developed by the wick structure to be greater than the capillary pressure ΔP_c. This condition defines the maximum heat transfer capability of the FHP, expressed as $\Delta P_{c,max} > \Delta P_c$. If this pressure balance is not satisfied, the FHP performances break down, and the heat transfer limitation, usually called the capillary or hydrodynamic limit, is reached. The maximum capillary pressure head

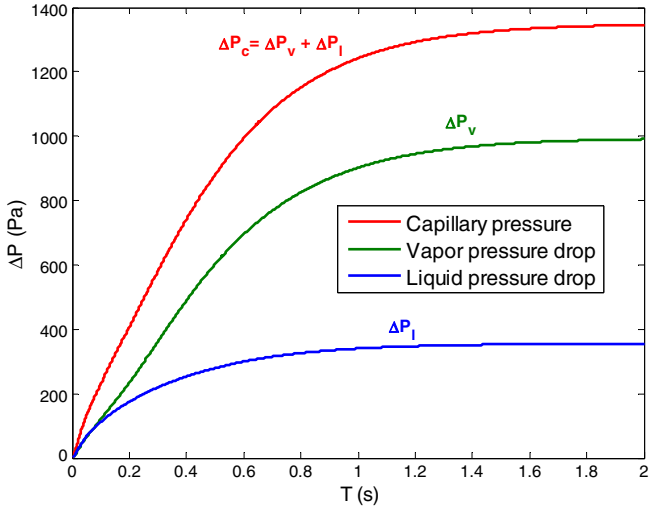

Fig. 13. Transient pressure drop inside the FHP during the start-up operation considered.

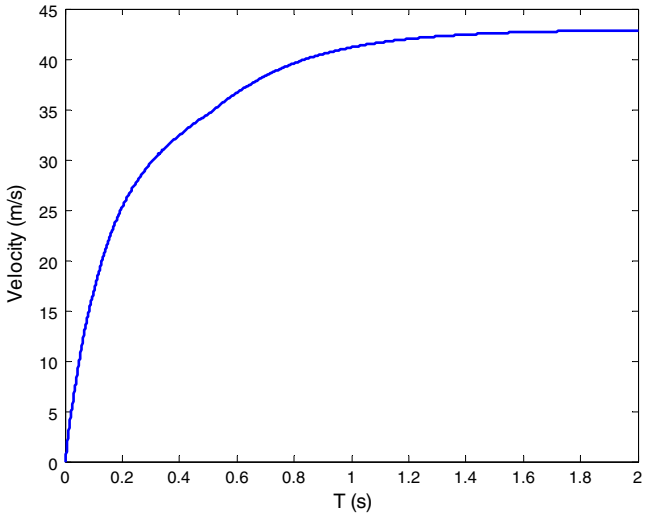

Fig. 15. Transient evolution of the maximum velocity in the vapor core.

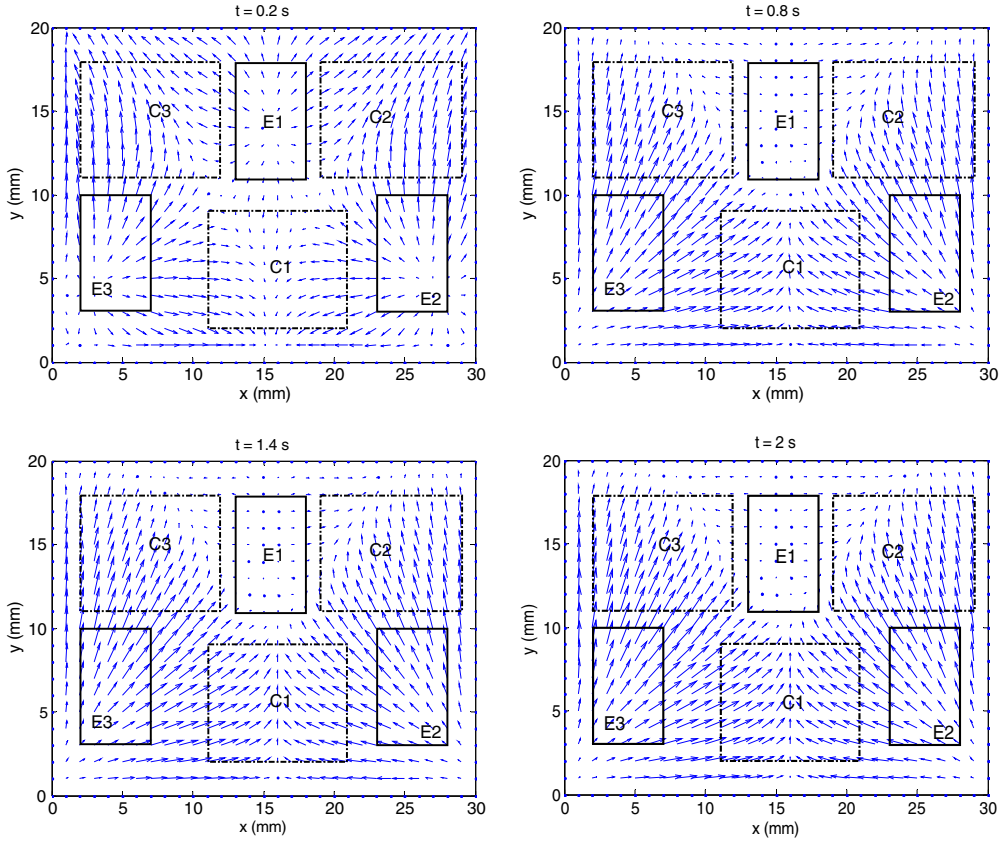

Fig. 14. Vapor velocity field (m/s) at different elapsed times.

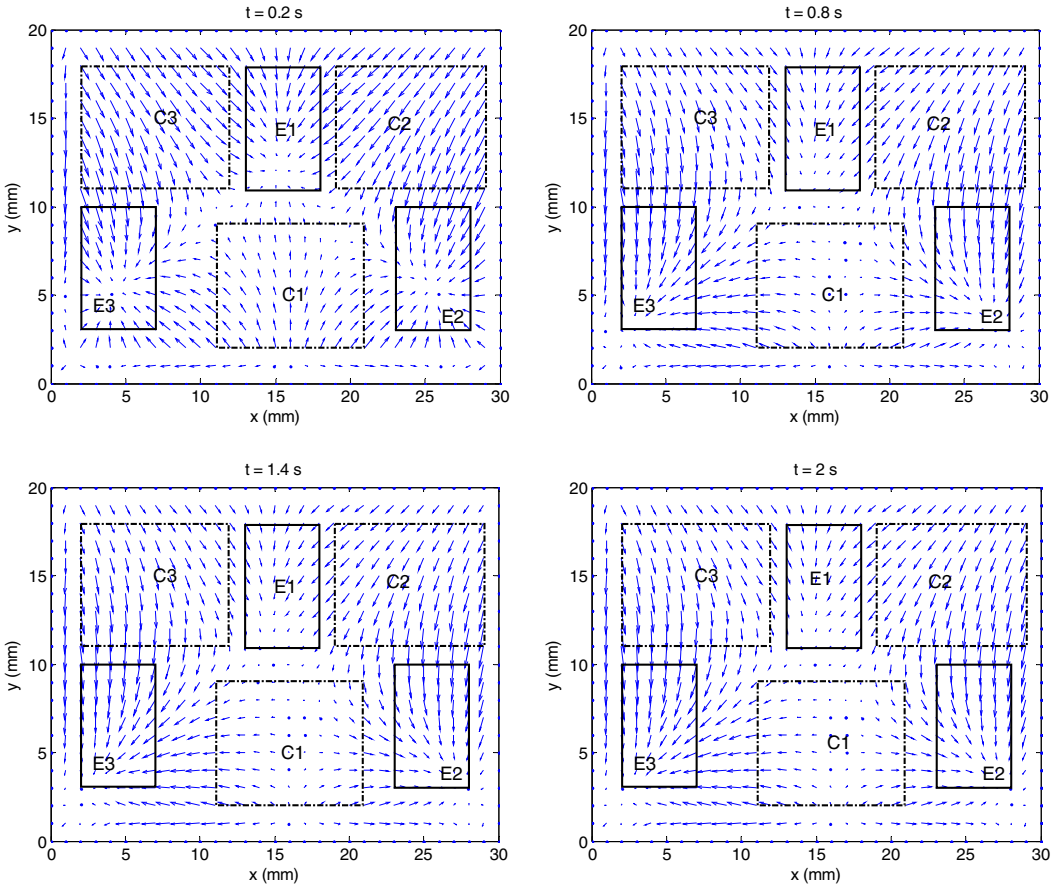

Fig. 16. Liquid velocity field (m/s) at different elapsed times.

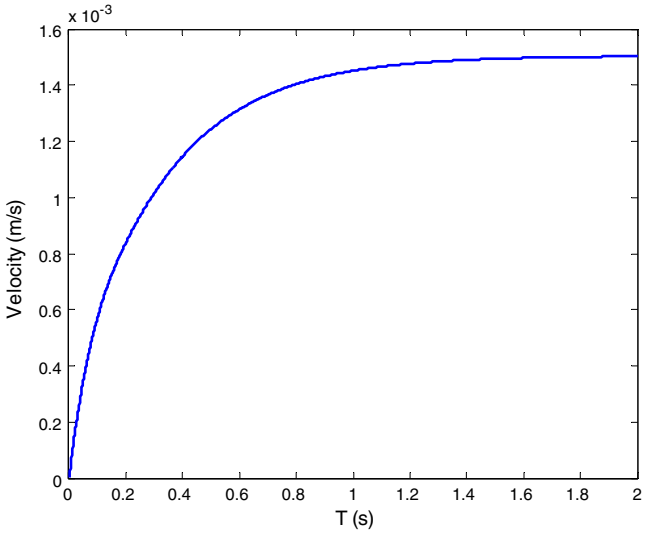

Fig. 17. Transient evolution of the maximum liquid velocity.

can be calculated using the classic expression of the Young–Laplace law: $\Delta P_{c,max} = 2\sigma/r_{eq}$.

The transient pressure drops inside the FHP are presented in Fig. 13. At the end of the cycle ($t = 2$ s), the vapor pressure losses are about $\Delta P_v = 990$ Pa and liquid pressure losses are about $\Delta P_l = 355$ Pa, corresponding to a capillary pressure of $\Delta P_c = 1345$ Pa. During the transient operation, the capillary limit is not reached since the maximum capillary pressure head is about $\Delta P_{c,max} = 4\,071$ Pa.

Fig. 14 shows the vapor velocity field inside the FHP at elapsed times of 0.2, 0.8, 1.4 and 2 s. The vapor velocity distribution illustrates that vapor is generated under the electronic components and flows in the direction of the condensers. The maximum velocity is located between the electronic component E_3 and the condenser C_3 at the shortest distance between this component and the condensers. For the elapsed times considered, Fig. 15 provides the maximum velocity value maximum. At the end of the transient operation ($t = 2$ s), the maximum vapor velocity is about 43 ms^{-1}, which corresponds to a maximum Reynolds number of around 67 and to a Mach number of 0.06. The characteristic dimension in the calculation of the Reynolds number is equal to two times the thickness of the vapor core. Thus, the assumption of laminar flow in the T2DHM model was well founded. In addition, since the maximum Mach number is inferior to the critical Mach number (unit), the FHP sonic limitation is not reached during the considered transient period.

The contour of the liquid velocity field is presented in Fig. 16 at the elapsed times of 0.2, 0.8, 1.4 and 2 s. Like the liquid pressure distribution, the liquid velocity distribution moves in the opposite direction from the vapor distribution. The liquid flow moves from the condensers towards the electronic components. The liquid velocity field shows that the liquid velocity increases from condenser zones and decreases after reaching the heating zones (i.e., under the electronic components). The maximum velocity occurs under the zone between the C_3 condenser and the E_3 component. Fig. 17 shows the evolution of the maximum velocity throughout

the transient operation. At the end of the considered start-up operation (t = 2 s), the maximum liquid velocity is about 1.5 10^{-3} ms^{-1}.

4. Conclusion

Two transient models were combined to predict the transient performances of a FHP by coupling the FHP wall heat transfer calculation to the fluid flow in both vapor and liquid phases. The FHP was used to cool multiple electronic components during a transient operation. The flow mechanisms in both the liquid and vapor phases were determined with a transient 2D hydrodynamic model, coupled to a transient 3D thermal model, which provides the heat transfer through the FHP wall. The thermodynamic effects due to the phase change mechanisms were also included. The steady-state results correspond well with previous results published in the literature. The ability of the FHP to act as a heat spreader is highlighted through a comparison of computational results for a solid copper plate. The results demonstrate that the FHP clearly works as a thermal spreader, providing a more uniform temperature distribution than the solid plate. The calculated pressure drop in the both phases show that the capillary limit is not reached, which means that the heat pipe is in the correct range of operation during the transient stage studied.

As the perspective of this work, an experimental investigation will be performed in order to provide the assessment of the model compared to experimental data.

References

[1] G. Pandraud, Étude expérimentale et théorique de micro caloducs en technologie silicium, Ph.D. thesis, Institut National des Sciences Appliquées de Lyon, France, 2004.
[2] F. Lefèvre, M. Lallemand, Coupled thermal and hydrodynamic models of flat micro heat pipes for the cooling of multiple electronic components, Int. J. Heat Mass Transfer (49) (2006) 1375–1383.
[3] X.Y. Huang, C.Y. Liu, The pressure and velocity fields in the wick structure of a localized heated flat plate heat pipe, Int. J. Heat Mass Transfer 39 (6) (1996) 1325–1330.
[4] G. Carbajal, C. B Sobhan, G. P Peterson, Dimensionless governing equations for the vapor and liquid flow analysis of heat pipes, J. Thermophys. Heat Tr. 20 (1) (2006) 140–144.
[5] A. Bejan, Heat Transfer, Wiley, 1993.
[6] G. Carbajal, C. B Sobhan, G.P. "Bud" Peterson, D.T. Queheillalt, Haydn N.G. Wadley, A quasi-3D analysis of the thermal performance of a flat heat pipe, Heat Mass Transfer 50 (21–22) (2007) 4286–4296.
[7] C.A.J. Fletcher, Computational Techniques for Fluid Dynamics, second ed., Springer-Verlag, Sydney, 1991 (pp. 330–374).
[8] A. Faghri, Heat Pipe Science and Technology, Taylor & Francis, 1994. pp. (821–835).